

Fiber draw synthesis

Nicholas D. Orf^{a,b}, Ofer Shapira^a, Fabien Sorin^{a,b}, Sylvain Danto^a, Marc A. Baldo^c, John D. Joannopoulos^d, and Yoel Fink^{a,b,1}

^aResearch Laboratory of Electronics, ^bDepartment of Materials Science and Engineering, ^cDepartment of Electrical Engineering and Computer Science, and ^dDepartment of Physics, Massachusetts Institute of Technology, 77 Massachusetts Avenue, Cambridge, MA 02139

Contributed by John D. Joannopoulos, January 24, 2011 (sent for review December 22, 2010)

The synthesis of a high-melting temperature semiconductor in a low-temperature fiber drawing process is demonstrated, substantially expanding the set of materials that can be incorporated into fibers. Reagents in the solid state are arranged in proximate domains within a fiber preform. The preform is fluidized at elevated temperatures and drawn into fiber, reducing the lateral dimensions and bringing the domains into intimate contact to enable chemical reaction. A polymer preform containing a thin layer of selenium contacted by tin–zinc wires is drawn to yield electrically contacted crystalline ZnSe domains of sub-100-nm scales. The in situ synthesized compound semiconductor becomes the basis for an electronic heterostructure diode of arbitrary length in the fiber. The ability to synthesize materials within fibers while precisely controlling their geometry and electrical connectivity at submicron scales presents new opportunities for increasing the complexity and functionality of fiber structures.

flexible electronics | optical fiber processing | semiconductor device

Thermal fiber drawing is a process in which a macrostructured preform is heated and drawn into extended lengths of microstructured fiber. New methods of increasing both the structural complexity of fibers and number of materials compatible with the drawing process are substantially expanding the functionality of photonic crystal and semiconductor device fibers (1–3). The drawing process, however, has until now been limited to materials that flow at the draw temperature. Approaches that attempt to circumvent this limitation include depositing materials inside (4–7) or onto the surface (8–11) of previously drawn fiber substrates. These methods do not take full advantage of the scaling associated with fiber drawing and are limited in their geometric complexity and the length over which uniform structures can be produced. Here this seemingly fundamental limitation is lifted by utilizing the fiber drawing process to synthesize in situ a chemical compound that has a melting temperature far exceeding the draw temperature. In this process, precursors are arranged in adjacent domains in a macroscopic preform. During thermal drawing, the fluid reactants come into contact and precipitate a new compound. To demonstrate the potential of this fiber draw synthesis method, a polymer fiber preform containing a thin selenium–sulfur layer next to eutectic tin–zinc wires is constructed and thermally codrawn into a fiber consisting of electrically contacted crystalline ZnSe domains of sub-100-nm scales at the interface between the metallic domains and selenium layer. The formation of the interface compound is the basis for an electronic heterostructure and a thermally drawn fiber device exhibiting rectifying behavior. The ability to synthesize materials during the fiber draw process while maintaining precise and arbitrary geometries should lead to substantial advances in the form and function of fibers.

Results and Discussion

A fiber preform consisting of metallic Sn₇₄Pb₂₆ and Sn₈₅Zn₁₅ wires placed within an amorphous polymer cladding and spanned by a thin film of Se₉₇S₃ was constructed and drawn into an extended fiber (schematic drawings and SEM micrographs of the preform and fiber are shown in Fig. 1). The metal electrodes were placed in an alternating fashion such that each Sn₇₄Pb₂₆/

Se₉₇S₃/Sn₈₅Zn₁₅ combination forms an independently addressable electronic device. Neither the elemental selenium nor zinc reactants are liquid at the drawing temperature and thus incompatible with thermal drawing. However, the melting temperature of both reactants can be depressed by alloying with either sulfur (in the case of selenium) or tin (for the zinc reactant). Upon exiting the drawing furnace, the selenium alloy is quenched into the amorphous state, but it easily devitrifies to the equilibrium crystalline phase when annealed for 1 h at 150 °C (12) (see *Methods* for full experimental details). The distance between the metal electrodes in a single fiber device is approximately 15 μm, an order-of-magnitude smaller than previous composite device fibers, suggesting that significant device miniaturization and concomitant increases in device performance and density are possible in future fiber devices (13).

The fiber diode optoelectronic properties are detailed in Fig. 2. The current-voltage characteristics per unit fiber length as a function of voltage both in the dark and under illumination from an AM1.5G solar source is given in Fig. 2A. The Sn₇₄Pb₂₆ electrode is biased positive with respect to the Sn₈₅Zn₁₅ electrode in the forward direction (Fig. 2A, *Inset*). Rectifying behavior is clearly evident in the dark, the magnitude of which is limited by the device series resistance arising from the lateral photodiode geometry. A short-circuit current and open-circuit voltage (0.5 V) develops under illumination, demonstrating the existence of an internal electric field and suggesting future application as a distributed photovoltaic device. A plot of the inverse square capacitance versus applied bias reveals a built-in voltage of about 0.8 V (Fig. 2B). The sign of the applied bias in *I*–*V* and *C*–*V* measurements suggests that the Se₉₇S₃/Sn₇₄Pb₂₆ junction behaves ohmically and the Se₉₇S₃/Sn₈₅Zn₁₅ is rectifying. The spectral responsivity shown in Fig. 2C under reverse bias (–2 V) shows maximum response at 460 nm (corresponding to an external quantum efficiency of 2%) and a trail off at around 650 nm, consistent with a selenium bandgap of 1.9 eV. This fiber diode structure represents a major improvement over previous thermally drawn photoconductor fiber devices. In addition to the newly observed rectification, the noise-equivalent power (NEP) of this structure is 1,000 times smaller than previous multimaterial thin-film photoconductor devices at 4.7 pW-Hz^{0.5} (14).

The *I*–*V* and *C*–*V* characteristics suggest that the metal-semiconductor-metal fiber device is single sided, i.e., composed of one ohmic and one blocking barrier. This is a surprising result because of the large work function difference between the semiconductor (15) and metals (16) and the fact that selenium is known to readily form rectifying barriers when contacted to metals in planar devices (17). Indeed in our own control experiments, thermally deposited selenium devices readily formed rectifying contacts, but until now all fiber devices behaved ohmically

Author contributions: N.D.O., O.S., F.S., S.D., M.A.B., J.D.J., and Y.F. designed research; N.D.O., O.S., F.S., and S.D. performed research; N.D.O., O.S., F.S., S.D., M.A.B., J.D.J., and Y.F. analyzed data; and N.D.O., O.S., F.S., S.D., M.A.B., J.D.J., and Y.F. wrote the paper.

The authors declare no conflict of interest.

¹To whom correspondence may be addressed. E-mail: yoel@mit.edu or joannop@mit.edu.

This article contains supporting information online at www.pnas.org/lookup/suppl/doi:10.1073/pnas.1101160108/-DCSupplemental.

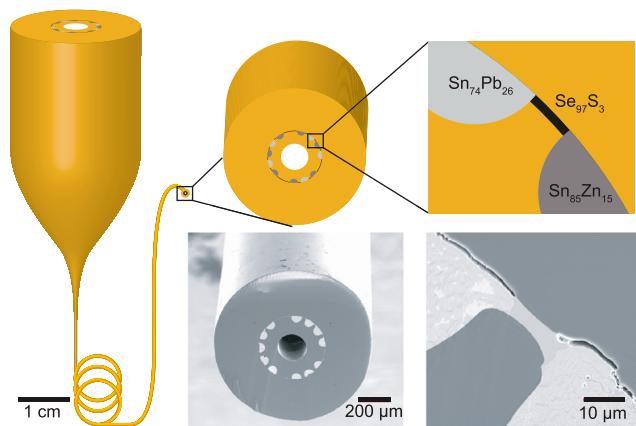


Fig. 1. Schematic drawings of structured preform drawn into fiber along with SEM micrographs of actual fiber and magnification of a single metal-semiconductor-metal device.

(see *SI Text*). The disparity in the electrical behavior between the planar and fiber devices is due to the different processing methods. Whereas fiber devices experience long periods of time at elevated temperatures where molecular diffusivity is high during preform fabrication and fiber drawing, the thermal evaporation techniques used to fabricate the planar devices are essentially room temperature processes. As the range in work function and elemental composition of the control planar devices spans and includes that of the fiber devices, it is clear that the electronic behavior of fiber devices is not controlled by work function difference. In fact, Kelvin probe force microscopy (KPFM), energy dispersive spectroscopy (EDS) compositional analysis, and Raman spectroscopy provide direct evidence of the formation of a ZnSe compound at the interface between Se_{97}S_3 and $\text{Sn}_{85}\text{Zn}_{15}$, and it is this interface compound that distinguishes the rectifying junction from previous metal-semiconductor-metal fiber devices.

The spatial variation in surface potential was measured by KPFM (18) and compared with compositional measurements performed by EDS. Fig. 3 presents the KPFM measurements (*i-iii*) along with SEM-based EDS line scans of similar junctions (*iv*). KPFM measured topography (*i*) and work function maps (*ii*) are shown as well as representative line scans (*iii*). Changes in height at interfaces arise from differences in sputter rates of the metals and semiconductor (19). A sharp change in both topography and work function can be seen at the $\text{Sn}_{74}\text{Pb}_{26}/\text{Se}_{97}\text{S}_3$ metallurgical interface (Fig. 3A). The KPFM map and line scan shows the potential change occurs over a 400-nm region

at this interface. The SEM EDS measurements reveal notable diffusion of tin and selenium across the interface as well as a small increase in the concentration of lead at the interface. In contrast, the band bending extends over 1 μm at the $\text{Se}_{97}\text{S}_3/\text{Sn}_{85}\text{Zn}_{15}$ interface (Fig. 3B), beginning with an abrupt change in contact potential at the 2.5- μm mark and followed by a more gradual change. The topography map, however, reveals the apparent metallurgical $\text{Se}_{97}\text{S}_3/\text{Sn}_{85}\text{Zn}_{15}$ junction does not coincide with this change in potential but rather occurs at the 1.1- μm mark. SEM EDS line scans show a large increase in zinc concentration at the metallurgical interface. Additional high-resolution scanning transmission electron microscope EDS measurements of mixed $\text{Se}_{97}\text{S}_3/\text{Sn}_{85}\text{Zn}_{15}$ interfaces generated under the same drawing conditions are given in the *SI Text*. These measurements show the zinc-containing regions coincide with the selenium-sulfur regions rather than the tin-containing regions even though zinc was initially separate from the sulfur-selenium regions prior to drawing. Furthermore, several point scans show zinc and selenium appearing in a one-to-one ratio.

The combination of the EDS and KPFM data suggest that the electronic behavior at the metal-semiconductor interfaces in the drawn fiber devices is guided by diffusion or compound formation between the metal and semiconductor components. The $\text{Se}_{97}\text{S}_3/\text{Sn}_{74}\text{Pb}_{26}$ junction behaves ohmically despite the large potential drop observed on the Se_{97}S_3 side of the junction by KPFM. EDS demonstrates that this interface is diffuse. Indeed the formation of a diffuse interface is a classic method of creating ohmic contacts between metals and semiconductors (20). The $\text{Se}_{97}\text{S}_3/\text{Sn}_{85}\text{Zn}_{15}$ interface is more interesting. A potential gradient across the region in Fig. 3B between 1.1 and 2.5 μm is clearly visible, but the region does not have the same topography as the selenium semiconductor and, in fact, appears as though it has a similar topography to the metal. As band bending cannot occur in high carrier density metals, this area must instead consist of a new semiconductor. If this potential change were due to only interface doping of the semiconductor, the bending would originate at the metal-semiconductor interface and extend only into the semiconductor, as is the case for the $\text{Se}_{97}\text{S}_3/\text{Sn}_{74}\text{Pb}_{26}$ junction in Fig. 3A. Based on the elements present at the interface, this compound can only be composed of some combination of SnSe, SnSe_2 , or ZnSe. The coincidence of zinc and selenium in the EDS measurements suggest that the compound is likely ZnSe based. Indeed, rectifying behavior cannot be controlled by SnSe or SnSe_2 because the small potential barrier that would develop between selenium [$E_g = 1.9$ eV, ionization potential (IP) = 5.9 eV; refs. 17 and 21] and these compounds (SnSe_2 , $E_g = 1.0$ eV, IP = 6.1 eV, ref. 22; SnSe, $E_g = 0.9$ eV, ref. 23, IP = 5.6 eV, ref. 24) cannot explain the built-in potential of

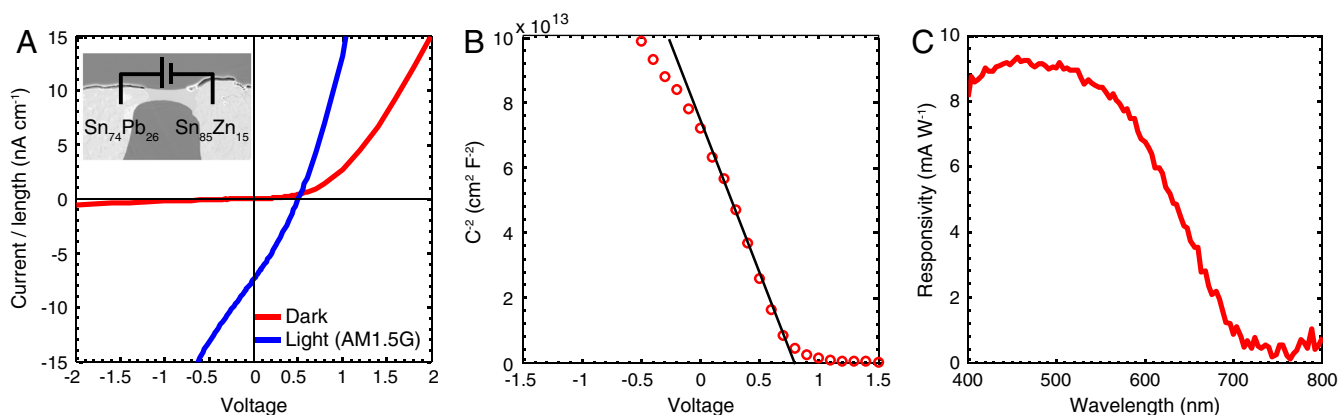


Fig. 2. Characterization of fiber-integrated photodiode. (A) Current per length for distributed photodiode in the dark and under illumination from simulated AM1.5G source. (*Inset*) Shows bias polarity. (B) Inverse square of capacitance as a function of applied voltage reveals a junction built-in voltage of 0.8 V. (C) Responsivity as a function of wavelength.

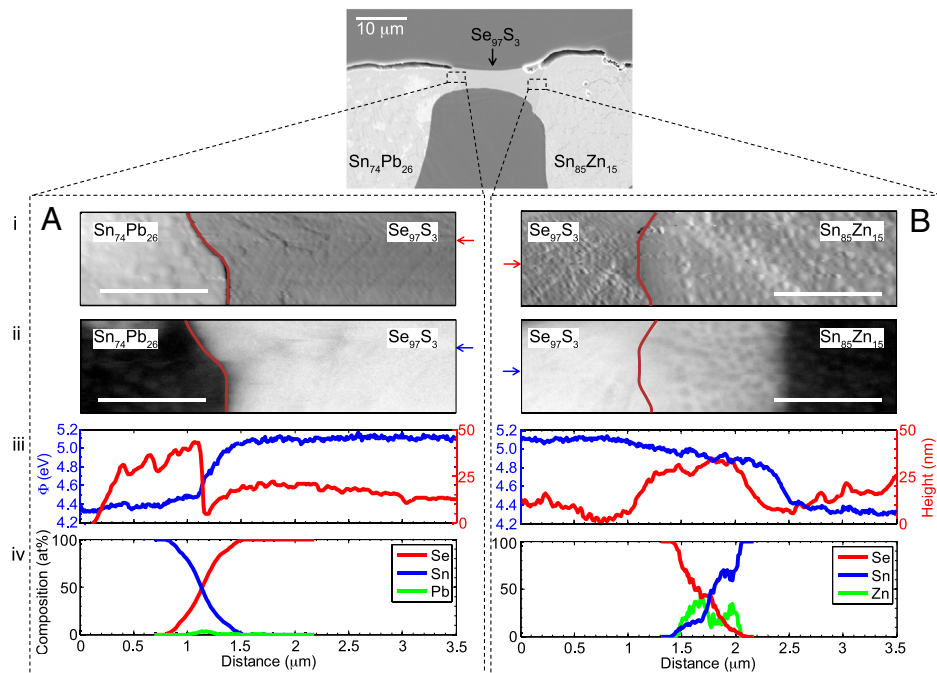


Fig. 3. Surface potential and chemical composition of $\text{Se}_{97}\text{S}_3/\text{Sn}_{74}\text{Pb}_{26}$ (A) and $\text{Se}_{97}\text{S}_3/\text{Sn}_{85}\text{Zn}_{15}$ (B) junctions. KPFM-measured topography and work function maps are shown in *i* and *ii*, respectively. Maroon lines highlight the metallurgical interface between metal and semiconductor. Colored arrows correspond to location of line scans in *iii*. EDS line scans show variation in composition across the metallurgical junction in *iv*. (Scale bar: 1 μm .)

0.8 V determined by both C - V and KPFM measurements. Furthermore there were no signs of this compound formation at the $\text{Se}_{97}\text{S}_3/\text{Sn}_{74}\text{Pb}_{26}$ interface even though SnSe and SnSe_2 would be just as likely to form at either interface due to the equally high concentration of tin and selenium at both junctions. A large bandgap semiconductor such as zinc selenide ($E_g = 2.7$ eV, IP = 6.8 eV) (25) would, however, form a barrier to hole conduction and explain the rectifying behavior. Additional macroscopic X-ray diffraction measurements performed on zinc pieces incubated in molten selenium at the fiber drawing temperature (260 °C) confirm that crystalline ZnSe can form at the drawing temperature (see *SI Text*).

Scanning confocal Raman microscopy performed on a drawn fiber provide direct evidence of ZnSe compound formation inside the fiber. Raman images of a small Se_{97}S_3 region that became mixed within the larger $\text{Sn}_{85}\text{Zn}_{15}$ metal matrix during fiber drawing are shown in Fig. 4. This area highlights the existence of an interfacial compound completely encompassing the Se_{97}S_3 area. Fig. 4*A*–*C* shows intensity maps obtained by integrating the spectral ranges 200–215, 230–245, and 248–263 cm^{-1} , corresponding to the three discrete peaks visible in the Raman spectra at 207, 238, and 252 cm^{-1} , respectively. Fig. 4*D* shows individual Raman spectra at five locations within the 5×5 - μm scan area. The high-intensity peak observed at location 1 (238 cm^{-1}) corresponds to the A_1 bond-stretching mode of trigonal selenium, the most thermodynamically stable of selenium allotropes (26), whereas the peaks at 207 and 252 cm^{-1} clearly seen in the spectra taken at locations 2, 3, and 4 correspond to the transverse optical and longitudinal optical modes of ZnSe, respectively (27). Location 5 in Fig. 4 corresponds to the $\text{Sn}_{85}\text{Zn}_{15}$ matrix, from which no Raman signal was observed. The broadband signal observed between approximately 160 and 550 cm^{-1} is due to semiconductor fluorescence. Several shoulders visible in the Raman spectra in Fig. 4*D* may imply the presence of ZnSe in Se_{97}S_3 and vice versa. Although these shoulders may indicate mixing of the selenium and ZnSe phases, they most likely appear because the semiconductor domains are on the order of the microscope resolution. Indeed, the presence of substantial Se_{97}S_3 within

ZnSe would result in electrical short-circuiting not seen in electronic characterization. Taken together, Fig. 4 clearly shows the presence of an interfacial region between the $\text{Sn}_{85}\text{Zn}_{15}$ matrix and Se_{97}S_3 particle, and this interfacial region is composed primarily of ZnSe. This result is consistent with the KPFM measurements, which also found the existence of an interfacial compound between $\text{Sn}_{85}\text{Zn}_{15}$ and Se_{97}S_3 .

A preliminary band diagram of the proposed $\text{Se}_{97}\text{S}_3/\text{ZnSe}/\text{Sn}_{85}\text{Zn}_{15}$ heterostructure is shown in Fig. 5. The diagram is constructed by combining the observed change in local vacuum

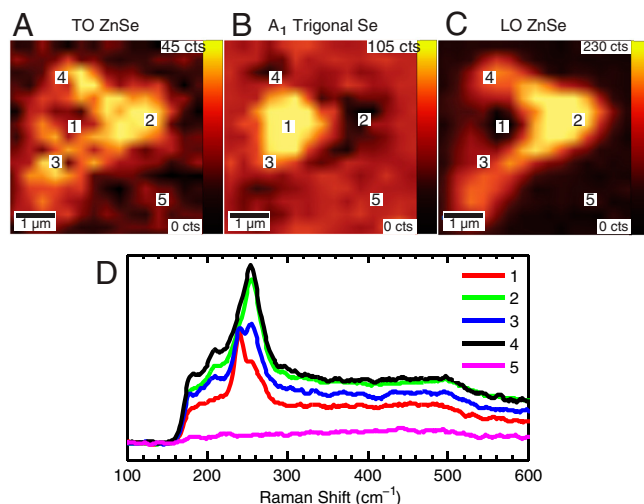


Fig. 4. Scanning Raman spectroscopy images of a Se_{97}S_3 particle surrounded by a $\text{Sn}_{85}\text{Zn}_{15}$ matrix within a drawn fiber. (A–C) Raman images obtained by integration of the spectral range 200–215, 230–245, and 248–263 cm^{-1} corresponding to the transverse optical (TO) ZnSe (207 cm^{-1}), A_1 bond stretching of trigonal Se (238 cm^{-1}), and longitudinal optical (LO) ZnSe modes (252 cm^{-1}), respectively. (D) Raman spectra recorded at locations 1–5 in parts A–C. Location 1 corresponds to the Se_{97}S_3 region. Locations 2–4 correspond to the ZnSe interfacial region. Location 5 corresponds to the $\text{Sn}_{85}\text{Zn}_{15}$ matrix.

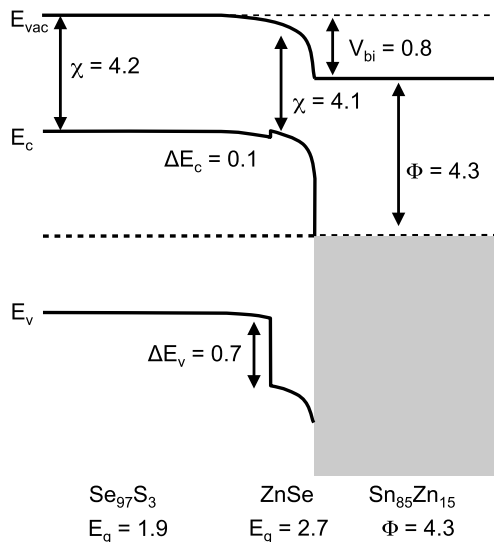


Fig. 5. Proposed band diagram of the $\text{Se}_{97}\text{S}_3/\text{ZnSe}/\text{Sn}_{85}\text{Zn}_{15}$ heterostructure (values in electronvolts).

level (i.e., contact potential) by KPFM with band offsets and built-in voltage calculated by Anderson's model of heterostructures given the material's bandgap and electron affinity (20, 28). The band diagram clearly indicates how the large discontinuity in the valence band at the $\text{Se}_{97}\text{S}_3/\text{ZnSe}$ interface would create a barrier to hole flow, and the estimated valence band discontinuity between Se_{97}S_3 and ZnSe of 0.7 eV is nearly equal to the observed built-in voltage of 0.8 eV. There is expected to be negligible difference between ZnSe and a statistical $\text{ZnS}_{0.03}\text{Se}_{0.97}$ alloy in either the Raman spectrum (29) or electronic bandgap (30), and the effect of local composition fluctuations would be minimal.

Conclusions

The ability to synthesize specific materials in specific locations within thermally drawn fibers represents a significant advance in fiber processing and suggests that many more materials can be built into composite fibers than previously thought. Zinc selenide, for example, has many interesting optical and electronic properties (31), but its high melting temperature (1,530 °C) previously precluded it from use in all types of thermal drawing. It is likely that other compound semiconductors may be incorporated into fibers with a similar method. One must simply identify materials that may be codrawn together that could react to form a new composition. The present work shows that metal chalcogenide semiconductors can be synthesized during fiber drawing. Given recent advances in the areas of silicon- and germanium-based fibers, it is likely that compound semiconductors used in conventional microelectronics may also be incorporated into photonic or electronic fiber devices. The fabrication of rectifying devices within drawn fibers by synthesis of an interface compound itself is an important development and is perhaps reminiscent of the first recognition that metal silicides can substantially improve the repeatability and reliability of metal-silicon contacts (32). This fiber photodiode exhibits a three-order-of-magnitude improvement in NEP over previous fiber photoconductor devices (14). Furthermore, the ability to form both ohmic and rectifying junctions is important for creating a host of different, increasingly complex electronic circuits. The ability to create blocking junctions may also be useful in improving the performance of newly

demonstrated fiber transistors (12), and this work should lay the groundwork for many advances in the function of fiber devices on both the individual and array level.

Methods

Fabrication. Se_{97}S_3 was synthesized from high-purity elements (Alfa Aesar) using the standard melt quenching technique. Elements in the correct proportion were inserted into a quartz ampoule under inert atmosphere and then transferred to a vacuum line for additional purification by sublimation of volatile oxides (approximately 2 h at 190 °C). The ampoule was then sealed and inserted into a custom rocking furnace where it was slowly heated to 500 °C and mechanically rocked overnight to ensure homogenization. The ampoule was then quenched in water and the glassy compound was removed.

Preforms were fabricated by first milling semicircular slots into the outer diameter of a polyethersulfone (PSU) polymer tube with a Bridgeport endmill. Slot spacing and orientation was kept constant with a digital indexer set to rotate the PSU tube at specific angles. High-purity wires of $\text{Sn}_{74}\text{Pb}_{26}$ and $\text{Sn}_{85}\text{Zn}_{15}$ at. % ($\text{Sn}_{63}\text{Pb}_{37}$ and $\text{Sn}_{91}\text{Zn}_9$ wt %) from Indium Corporation were cut in half lengthwise and tightly fitted into the milled slots. A thick film (approximately 30 μm) of semiconductor was thermally evaporated onto a PSU substrate and then wrapped around the preform core so that the semiconductor and metal electrodes were touching. Additional layers of PSU were then wrapped around the devices to impart mechanical toughness. The resulting preform was fused into a single solid structure by heating under vacuum at 230 °C for 1 h and then slowly cooled to room temperature. The completed preform (having dimensions 26 mm in diameter, 120 mm in length) was then taken to an optical draw tower where it was thermally drawn into approximately 35 m of continuous device fiber (nominal diameter approximately 1 mm) at 260 °C.

Characterization. Current-voltage measurements were performed with a Keithley 6517a electrometer. Capacitance measurements were performed with a Hewlett Packard 4284a LCR meter at 20 Hz and 50 mV swing voltage to include the effects of all potential long-lived trap states. Photocurrent was measured as a function of wavelength for monochromated light and normalized by the measured responsivity at 530 nm. The NEP at 530 nm was calculated from the responsivity and the photodiode noise (taken to be the reverse bias dark current). Samples for imaging and surface analysis were prepared by ion polishing with a JEOL cross-section polisher. Amplitude modulated KPFM was performed with an Omicron ultrahigh vacuum variable temperature atomic force microscope (base pressure $<5 \times 10^{-10}$ torr) equipped with a Kelvin probe control unit using a nanosensors Pt-Ir tip (nominal resonance ~ 75 kHz). Kelvin signal was run at the first overtone of cantilever resonance (approximately 475 kHz) with an applied peak-to-peak voltage of 200 mV to minimize tip-induced band bending. The tip work function was calculated by determining the contact potential difference (CPD) between the tip and a clean polycrystalline gold surface, and the sample work function was calculated by the relation $\Phi_{\text{tip}} - \Phi_{\text{sample}} = \text{CPD}$. Samples were cleaned in situ by argon-ion sputtering. The observed contact potential for both metal electrodes is consistent with previous work function measurements (16) and the measured work function of the selenium semiconductor appears in the middle of its known bandgap, giving confidence that the surface is reasonably well prepared and representative of the device's electronic structure. Image analysis was performed with SPIP and Gwyddion. Scanning confocal Raman spectroscopy was performed with a Witec CRM 200 in a backscatter geometry. A 532-nm laser was used as the excitation source and was focused onto the sample with a 100 \times NA0.9 objective.

ACKNOWLEDGMENTS. The authors wish to thank P. Jadhav, W. Melitz, and K. Celebi for help setting up the KPFM, W. DiNatalie and D. S. Yun for help with transmission electron microscopy measurements, S. Speakman for help with X-ray diffraction measurements, and J. Deng of the Harvard Center for Nanoscale Systems for help with Raman spectroscopy. N.D.O. gratefully acknowledges support from the National Defense Science and Engineering Graduate Program. This research was supported in part by the US Army Research Office through the Institute for Soldier Nanotechnologies at Massachusetts Institute of Technology (Contract W911NF-07-D-0004) as well as by the Materials Research Science and Engineering Center Program of the National Science Foundation (Award DMR-0819762).

- Russell P (2003) Photonic crystal fibers. *Science* 299:358–362.
- Abouraddy AF, et al. (2007) Towards multimerial multifunctional fibres that see, hear, sense and communicate. *Nat Mater* 6:336–347.
- Cerqueira SA (2010) Recent progress and novel applications of photonic crystal fibers. *Rep Prog Phys* 73:024401.

- Tyagi HK, Schmidt MA, Sempere LP, Russell PSJ (2008) Optical properties of photonic crystal fiber with integral micron-sized Ge wire. *Opt Express* 16:17227–17236.
- Shapira O, et al. (2006) Surface-emitting fiber lasers. *Opt Express* 14:3929–3935.
- Jackson BR, Sazio PJA, Badding JV (2008) Single-crystal semiconductor wires integrated into microstructured optical fibers. *Adv Mater* 20:1135–1140.

7. Sazio PJA, et al. (2006) Microstructured optical fibers as high-pressure microfluidic reactors. *Science* 311:1583–1586.
8. O'Connor B, Pipe KP, Shtein M (2008) Fiber based organic photovoltaic devices. *Appl Phys Lett* 92:193306.
9. Liu JW, Namboothiry MAG, Carroll DL (2007) Fiber-based architectures for organic photovoltaics. *Appl Phys Lett* 90:063501.
10. Liu JW, Namboothiry MAG, Carroll DL (2007) Optical geometries for fiber-based organic photovoltaics. *Appl Phys Lett* 90:133515.
11. Lee MR, et al. (2009) Solar power wires based on organic photovoltaic materials. *Science* 324:232–235.
12. Danto S, et al. (2010) Fiber field-effect device via in situ channel crystallization. *Adv Mater* 22:4162–4166.
13. Bayindir M, et al. (2005) Integrated fibres for self-monitored optical transport. *Nat Mater* 4:820–825.
14. Sorin F, et al. (2007) Multimaterial photodetecting fibers: A geometric and structural study. *Adv Mater* 19:3872–3877.
15. Lide DR (2008) *CRC Handbook of Chemistry and Physics* (CRC, New York), pp 12–114.
16. Orf N, Baikie I, Shapira O, Fink Y (2009) Work function engineering in low temperature alloys. *Appl Phys Lett* 94:113504.
17. Champness CH, Chan A (1985) Relation between barrier height and work function in contacts to selenium. *J Appl Phys* 57:4823–4825.
18. Sommerhalter C, Matthes TW, Glatzel T, Jager-Waldau A, Lux-Steiner MC (1999) High-sensitivity quantitative Kelvin probe microscopy by noncontact ultra-high-vacuum atomic force microscopy. *Appl Phys Lett* 75:286–288.
19. Seah MP, Clifford CA, Green FM, Gilmore IS (2005) An accurate semi-empirical equation for sputtering yields I: For argon ions. *Surf Interface Anal* 37:444–458.
20. Sze S (1981) *Physics of Semiconductor Devices* (Wiley Interscience, New York), 2nd Ed., pp 122–129, pp 304–306.
21. Williams RH, Polanco JI (1974) Electronic-structure of chalcogenide solids—photoemission study of ordered and disordered selenium and tellurium. *J Phys C: Solid State Phys* 7:2745–2759.
22. Schlaf R, Pettenkofer C, Jaegermann W (1999) Band lineup of a SnS₂/SnSe₂/SnS₂ semiconductor quantum well structure prepared by van der Waals epitaxy. *J Appl Phys* 85:6550–6556.
23. Madelung O, Rössler U, Schulz M, eds. (1998) *Tin Selenide (SnSe) Band Structure, Energy Gap, Effective Masses* (SpringerMaterials, New York), The Landolt-Börnstein Database, 41C.
24. Bennouna A, Priol M, Seignac A (1988) Experimental density of states of tin selenide measurement on thin-films. *Thin Solid Films* 164:69–73.
25. Chiang TC, Himpel FJ (2006) ZnSe. *Electronic Structure of Solids: Photoemission Spectra and Related Data, Landolt-Bornstein Group III*, eds A Goldmann and EE Koch (Springer Verlag, New York), Vol 23a, pp 81–84.
26. Nagata K, Ishibashi K, Miyamoto Y (1981) Raman and infrared-spectra of rhombohedral selenium. *Jpn J Appl Phys* 20:463–469.
27. Taylor W (1967) Raman Spectra of cubic zinc selenide and telluride. *Phys Lett A* 24:556–558.
28. Milnes AG, Feucht DL (1972) *Heterojunctions and Metal-Semiconductor Junctions* (Academic, New York), pp 1–43.
29. Gupta P, Bhattacharyya D, Chaudhuri S, Pal AK (1992) Preparation and characterization of polycrystalline Zn_xSe_{1-x} films prepared by a 2-zone hot wall technique. *Thin Solid Films* 221:154–159.
30. Ebina A, Fukunaga E, Takahashi T (1974) Variation with composition of E₀ and E₀+Delta-0 gaps in Zn_xSe_{1-x} alloys. *Phys Rev B: Condens Matter Mater Phys* 10:2495–2500.
31. Kale RB, Lokhande CD (2004) Room temperature deposition of ZnSe thin films by successive ionic layer adsorption and reaction (SILAR) method. *Mater Res Bull* 39:1829–1839.
32. Zhang S-L, Ostling M (2003) Metal silicides in CMOS technology: Past, present, and future trends. *Crit Rev Solid State Mater Sci* 28:1–129.